Large-eddy simulation and deduced scaling analysis of Rayleigh–Bénard convection up to $Ra = 10^9$**

S.-H. PENG*†§, K. HANJALIC‡ and L. DAVIDSON§

†Department of Computational Physics, Division of Systems Technology,
Swedish Defence Research Agency (FOI), SE-164 90 Stockholm, Sweden
‡Department of Multi-scale Physics, Delft University of Technology, 2600 GA Delft, The Netherlands
§Division of Fluid Dynamics, Department of Applied Mechanics,
Chalmers University of Technology, SE-412 96 Gothenburg, Sweden

Large-eddy simulation of turbulent Rayleigh–Bénard (RB) convection has been performed for a 6:1:6 open-ended domain for Rayleigh numbers ranging from 6.3×10^5 to 10^9 at Prandtl number of $Pr = 0.71$. The scaling analysis based on the LES data shows that the heat transfer follows a single relation of $Nu = 0.162Ra^{0.286}$, which is consistent with the scaling law for the hard turbulence regime reported in several earlier experimental and DNS studies. The present LES also supports some earlier experimental and DNS findings that most of characteristic parameters can be scaled reasonably well with Ra number in the considered Ra number range using a single relation. Nonetheless, it is found that the scaling of several quantities shows a sensible offset from a single relation, and could be fitted better with the separate scaling relations for the soft and hard convective turbulence transitioned at about $Ra = 4 \times 10^7$. It has been argued that the transition, reflected in the scaling relation, may be attributed to the increasing 'containing effect' of the plume leaving the horizontal wall on the plume approaching the wall at large Ra numbers in the near-wall region.

1. Introduction

Despite extensive theoretical, experimental and numerical studies (for detailed reviews see e.g. [1–3]), Rayleigh–Bénard (RB) problem, widely viewed as the paradigm of thermal convection, is still surrounded with controversies. The flow and thermal dynamics in RB convection depends on the geometrical setup, the temperature difference between the two horizontal boundaries and the fluid property, which have usually been cast into two dimensionless parameters, the Rayleigh number, $Ra = g\beta\Delta T_0 H^3/(\nu\alpha)$, and the Prandtl number, $Pr = \nu/\alpha$, where $\Delta T_0 = (T_h - T_c)$ and H are respectively the temperature difference and the distance between the hot (T_h) and cold (T_c) horizontal surfaces, ν is the molecular kinematic viscosity and α the thermal diffusivity of the fluid.

The dependence of the dynamic and thermal quantities on the Ra and Pr numbers is of particular interest in RB convection, of which the Ra scaling of heat transfer (in terms of Nusselt number, Nu) has been perhaps most studied. A number of experiments, conducted

---

*Corresponding author. E-mail: peng@foi.se

usually in a closed cylindrical or rectangular small-aspect-ratio containers reported the classical $Nu \propto Ra^{1/3}$ scaling. For example, Deardorff and Willis [4] detected in their experiment the $Ra^{1/3}$ scaling for Ra number up to 10^7. Later, Sano et al. [5], Wu and Libchaber [6] and others from the Chicago group, in experiments with different aspect ratios, found that the heat flux obeys the classic $Ra^{1/3}$ scaling law only at lower Ra numbers. This scaling regime was termed *soft* convective turbulence. With increasing Ra number to $Ra = 4 \times 10^7$ and higher, the soft turbulence evolves into the so-called *hard* convective turbulence regime, characterized by different plume structure, temperature probability distribution in the core region (nearly exponential instead of Gaussian) and following a $Ra^{2/7}$ scaling law for heat transfer. In contrast to this, Chu and Goldstein [7] reported a consistent scaling of their measured Nu with $Ra^{0.278}$, which is very close to the 'hard' regime scaling, for the whole range of $2.76 \times 10^5 \leq Ra \leq 1.05 \times 10^8$ covering basically the soft regime and a little beyond it.

Numerical simulations, with all its potential, are expected to clarify the experimental differences and bring more insight into the physics of the various convective regimes. A comprehensive analysis by Kerr [8] using well-resolved direct numerical simulations (DNS) for Ra numbers $5 \times 10^5 \leq Ra \leq 2 \times 10^7$ (which also provides an overview of several earlier DNS) showed that the heat transfer follows a single regime with hard-convection scaling, $Nu \propto Ra^{0.28}$, for the whole Ra number range considered. Later, Kerr and Herring [9] conducted DNS on Prandtl number dependence in the range of $0.07 \leq Pr \leq 7.0$ for $10^4 \leq Ra \leq 10^7$. Different scaling relations were reported at low-Prandtl numbers. Kerr [8] has argued that different regimes detected in experiments (soft) and in numerical simulations (hard) for the same range of Ra numbers can originate from differences in the setup geometry (e.g. the shape and aspect ratio) and boundary conditions, among which the most influential are the rigid side walls in the experimental research as compared with the open boundaries in numerical simulations. Because the proper DNS of RB convection with side walls are confronted with insurmountable grid resolution problems for higher Ra numbers, it is sometimes termed 'numerical RB convection' to distinguish it from experimental situations in enclosures.

As demonstrated by Kerr, DNS can provide full information on all flow properties up to the finest dissipative scale. Because of extreme requirements on computer resources, however, DNS is limited to relatively low Ra numbers, currently aiming at $Ra \approx 10^8$. For higher Ra numbers, large-eddy simulation (LES) has been considered as the only viable option. LES can provide full insight into the large-scale convective and turbulence structures at much higher Ra numbers. However, for capturing accurately the near-wall turbulence structure, heat transfer and shear, the near-wall grid-resolution restriction similar to those for DNS has limited at present the possibility to extend the Ra number range to only one or two decades. Several LES studies have been reported in the literature, but not all can be regarded as reliable for establishing or verifying the Ra-scaling laws. In an early LES for 4:1:4 domain, in which the Smagorinsky subgrid-scale (SGS) model was extended to account for buoyancy effects, Eidson [10] obtained a scaling relation of $Nu \sim Ra^{0.28}$ for $Ra \leq 2.5 \times 10^6$, but his simulations for higher Ra numbers, especially for $Ra = 10^8$, showed to be erroneous, most probably because of insufficient grid resolution. For $Ra \leq 10^8$, Kimmel and Domaradzki [11] examined their SGS estimation model in LES for the RB convection, where the heat transfer was over estimated as compared with DNS and experimental data.

To reach higher Ra numbers with numerical simulations, Kenjereš and Hanjalić [12, 13] applied the transient RANS (T-RANS) approach for Ra numbers up to 2×10^{16}. These simulations reproduced well the Nu–Ra scaling of Kerr's DNS, as well as several experimental data sets for much higher Ra numbers, showing after $Ra \approx 10^{14}$ also a trend toward the asymptotic regime of Kraichnan $Nu \to Ra^{1/2}$ for $Ra \to \infty$. However, because of inevitable empirical RANS model used for subscale motions, the T-RANS method cannot be trusted for

establishing or verifying any physical and scaling laws, but can serve for computations of high *Ra* number complex thermal convection of industrial relevance.

We present here LES of RB convection for *Ra* numbers in the range of $6.3 \times 10^5 \leq Ra \leq 10^9$, covering thus both the *soft* and *hard* convective turbulence regimes with a sufficient margin above the transitional *Ra* number. The main purpose of the work is to revisit some scaling relations in comparison with previous DNS results but for a broader *Ra* range. Effort has also been made to analyze the scaling of some dynamic and thermal properties and their *Ra* dependence in the soft and hard *Ra* number regions.

Because LES does not resolve the complete turbulence spectrum and requires an empirical model for the unfiltered subgrid-scale motion, its use for establishing scaling laws has been questioned, especially when wall phenomena are involved. For this reason, in order to provide credibility into the LES results, we consider first in detail the grid resolution criteria and the used subgrid-scale model. We move then to present and discuss the results.

2. Simulation methodology

Applying a spatial filtering to the governing equations for incompressible flows leads to additional subgrid-scale (SGS) stresses in the momentum equations, and extra SGS heat fluxes in the thermal energy equation, which must be modeled to close the equation system and to represent the effect of SGS turbulence on the resolved motion and scalar transport. The SGS model used in the present simulation is the dynamic Smagorinsky model, where the model coefficient is determined using the dynamic procedure [14, 15]. A similar procedure is applied to the computation of the thermal field [16], for which the gradient-diffusion hypothesis is employed to model the SGS heat fluxes. Both model coefficients, C_s for the SGS stresses and C_t for the SGS heat flux, have thus been determined as functions of time and space. However, in order to stabilize the numerical procedure, a spatial averaging over the homogeneous *x*- and *z*-directions has been employed in the dynamic procedure. These SGS model coefficients consequently vary only with time and in the inhomogeneous *y*-direction. The grid-filtered governing equations are discretized on a collocated grid using the second-order central differencing finite-volume method. The solution is advanced in time with the second-order Crank–Nicholson scheme. An implicit, fractional step method is used to solve the discretized equation system in conjunction with a multigrid pressure Poisson solver. The initial solution is generated from a coarse-grid solution at the same *Ra* number, being extrapolated to the refined grid. The time history of flow variables has been probed at some locations near the wall and in the center of the domain, which may give an indication of the flow- and thermal-field development with time. After both fields are fully developed (typically, one or two convective time scale), the statistical analysis is carried out over more than ten time scale, as will be further demonstrated in the following section. The statistic quantities (denoted by $\langle \cdot \rangle$) have been obtained by averaging the solutions in time and over the horizontal *x* and *z* homogeneous directions.

The computations have been carried out for a computational domain with rigid upper and lower boundaries at fixed temperature and periodic conditions at the open side boundaries. The aspect ratio of the numerical domain is $6 : 1 : 6$ ($A = 6$), which is the same as in the DNS by Kerr [8]. In a recent DNS study of RB convection by Hartlep et al. [17, 18], the dependence of properties on the aspect ratio, *A*, of the computational domain has been investigated for *Ra* numbers up to 10^7 using periodic boundary conditions in the horizontal directions. Hartlep et al. have employed aspect ratios up to $A = 10$ for a set of relatively large *Ra* numbers in their DNS. It is shown that for $Pr = 0.7$ and $Ra \leq 10^6$ the wavelength, λ_{max}, of large-scale structures holds in general $\lambda_{max} \leq 5$ [17], and that the Nusselt number exhibits insignificant

dependence on the aspect ratio ranging from $A = 5$ to $A = 10$ for $Pr = 0.7$ at, respectively, $Ra = 10^6$ and $Ra = 10^7$ [18]. Apart from their own DNS data in the analysis of $\lambda_{\max}$ as a function of Ra number, Hartlep et al. [17] have also compiled some existing experimental data measured in rectangular containers for Ra numbers up to about 3×10^7. At $Ra = 10^6$ and above, the experimental data give a constant value of $\lambda_{\max} \approx 6.3$, which is however larger than the numerical result from their DNS ($\lambda_{\max} = 5$ at $Ra = 10^6$). If large scales as such arise in numerical simulations, it is desired to have $A > \lambda_{\max}$ in order to avoid causing any possible truncation of large-scale structures.

It is however unclear whether such large scales would perserve at higher Ra numbers for 'numerical RB convection' where periodical conditions are imposed on the end side boundaries of the domain. According to Hartlep et al. [17], moreover, the large scales are 'continuations of the structures already present in laminar flows', and it is not justified whether the large-scale structures will disappear at high Ra numbers beyond their DNS. In the present LES computation, we have checked the two-point correlation in the homogeneous horizontal directions. It is noted that the correlation of resolved large-scale velocity components reduces from unity to zero over a range generally less than 25% of the horizontal size for a domain with $A = 6$. In addition, it should be noted that, if large-scale structures arise with a size larger than the computational domain, the time-averaging analysis may become troublesome to converge statistically independent properties. In this case, the turbulence statistics would shift from a symmetric/anti-symmetric vertical distribution varying with the averaging time. With the present computations, as will be illustrated below, such problems are not encountered in the statistical analysis. The computational domain with $A = 6$ as used in the present LES work should be justified as being appropriate.

The simulations were performed for Prandtl number $Pr = 0.71$ at five Rayleigh numbers, 6.3×10^5, 1.0×10^7, 4.0×10^7, 1.0×10^8 and 1.0×10^9. A set of relatively coarse meshes were used in the previous computation, from which the results have shown trends in Ra-scaling analysis that are generally in line with previous experimental and DNS investigations [19]. Nevertheless, as shown in table 1, the spatial resolution with these relatively coarse meshes is questionable at large Rayleigh numbers. Note that a uniform grid has been used in the homogeneous x- and z-directions, whereas non-uniform mesh spacing is used in the vertical y-direction with a clustered grid near the top and bottom walls. The parameter Δy_c indicates the vertical mesh spacing in the center of the computational domain and Δy_w is the near-wall spacing, both normalized with H. The time step, Δt, has been normalized with H and α. The Rayleigh number defined in the computations was varied by changing α.

Achieving the proper spatial resolution for numerical simulation of turbulent RB convection has been regarded as the key prerequisite to obtain the trustworthy results. For DNS, the grid size has in general been regarded as sufficiently fine when it is of the same order as the Kolmogorov length scale, $\eta = (\nu^3/\varepsilon)^{1/4}$, where ε is the dissipation rate of turbulence kinetic energy, [8, 20, 21]. Specifically, for $Pr \leq 1$ Grötzbach [20, 21] used the mesh size by $h \leq \pi \eta$.

Table 1. Simulation parameters with coarse grid resolutions.

Case	Ra	$N_x = N_z$	N_y	$\Delta x = \Delta z$	Δy_c	Δy_w	Δt
CA	6.3×10^5	48	64	0.1250	0.0301	0.0032	8.48×10^{-5}
CB	1.0×10^7	48	64	0.1250	0.0301	0.0032	2.13×10^{-5}
CC	4.0×10^7	64	80	0.0938	0.0278	0.0021	1.07×10^{-5}
CD	1.0×10^8	64	80	0.0938	0.0278	0.0021	0.68×10^{-5}
CE	1.0×10^9	64	96	0.0938	0.0263	0.0013	0.21×10^{-5}

Noting that the dimensionless kinetic energy dissipation is scaled with $(Nu - 1)Ra$, Kerr [8] has estimated the Kolmogorov length scale as

$$\eta/H = \sqrt{Pr}/[(Nu - 1)Ra]^{1/4}. \tag{1}$$

Consequently, the mean spacing, h, of the mesh in a DNS should comply with

$$\frac{h}{H} \leq \frac{\pi\sqrt{Pr}}{[(Nu - 1)Ra]^{1/4}}. \tag{2}$$

Unlike DNS, LES resolves only the filtered large scales on which the effect of unfiltered small scales is modeled by a subgrid-scale model. The use of the SGS model makes the spatial resolution relaxed, tolerating grid-cell size (i.e. filter width) larger than the Kolmogorov scale. A well-resolved LES should have the filtering cutoff located in the inertial subrange of the energy spectrum, where the unfiltered scales tend to be more isotropic so that the SGS turbulence can be assumed in constant spectral equilibrium. This thus suggests

$$\varepsilon \sim \varepsilon_{\text{sgs}} = \nu_{\text{sgs}}|\bar{S}|^2, \tag{3}$$

where ε_{sgs} is the SGS dissipation which represents the energy drain from the resolved to the SGS turbulence, ν_{sgs} is the SGS eddy viscosity and $|\bar{S}|$ is the magnitude of the resolved strain rate tensor. In the isotropic homogeneous case, one can write approximately

$$\langle|\bar{S}|^2\rangle = 2\int_0^{\kappa_c} \kappa^2 E(\kappa)\mathrm{d}\kappa, \tag{4}$$

where $\kappa_c = \pi/\Delta$ is the cutoff wavenumber and Δ is the filter width proportional to the mesh size, $\Delta = (\Delta x \Delta y \Delta z)^{1/3}$. Introducing $E(\kappa) = C_k\langle\varepsilon\rangle^{2/3}\kappa^{-5/3}$ into equation (4) gives

$$\langle|\bar{S}|^2\rangle = \frac{3}{2}C_k\langle\varepsilon\rangle^{2/3}\left(\frac{\pi}{\Delta}\right)^{4/3}, \tag{5}$$

where C_k is the Kolmogorov constant $C_k = 1.4 - 2.0$. Assuming that $\langle\varepsilon\rangle \simeq \langle\nu_{\text{sgs}}\rangle\langle|\bar{S}|^2\rangle$ [22], and using the relation of $\langle\varepsilon\rangle H^4/(\nu\alpha^2) = (Nu - 1)Ra$ in equation (5), leads to

$$\frac{\Delta}{H} \simeq \left(\frac{3}{2}C_k\right)^{3/4}\left(\frac{\langle\nu_{\text{sgs}}\rangle}{\nu}\right)^{3/4}\frac{\pi\sqrt{Pr}}{[(Nu - 1)Ra]^{1/4}}. \tag{6}$$

Equation (6) can be used to estimate the mean spatial resolution in LES for RB convection. As compared with the spatial resolution in DNS, equation (2), the LES resolution is further justified by $R_{\text{sgs}} = \langle\nu_{\text{sgs}}\rangle/\nu$. For $R_{\text{sgs}} < 1$, equation (6) gives an estimation comparable with the spatial resolution for DNS, namely, $\Delta \sim \eta$. In LES, the quantity ν_{sgs} represents the intensity of the unfiltered SGS turbulence, for which R_{sgs} should be as small as possible to attain a well-resolved LES, but not necessary to approach a DNS mesh resolution, the missing information being provided by the SGS model. In practice, a plausible argument is that $\langle\nu_{\text{sgs}}\rangle$ should preferably stay at about the same order as of ν, namely, $R_{\text{sgs}} \leq 10$. The mesh size used in table 1 has been estimated on the basis of such a criterion by taking the upper-bound value of R_{sgs}. Nonetheless, it seems that the mesh for higher Ra numbers is not fine enough to resolve the turbulent heat flux across the fluid layer. Effort has thus been made to further refine the mesh in this work. In addition, equation (6) implies that the mean SGS eddy viscosity increases in accordance with $\langle\nu_{\text{sgs}}\rangle \propto [(Nu - 1)Ra]^{1/3}$ with a certain filtering cutoff in the inertial subrange.

Apart from equation (6), an alternative way to estimate the spatial resolution in LES is to let the filtering cutoff width be justified with the Taylor microscale, λ, which for isotropic turbulence is expressed by $\lambda^2 = 15\nu u^2/\varepsilon$, where u is a velocity scale for large-scale structures

and can be estimated in terms of the resolved turbulence kinetic energy, K. Using the scaling for ε, we get

$$\frac{\lambda}{H} = \frac{\sqrt{15}u^*}{[(Nu-1)Ra]^{1/2}}, \tag{7}$$

where $u^* = \sqrt{K}H/\alpha$. In LES of isotropic turbulence, the mesh spacing has often been verified by using a value comparable to λ. We use $\lambda/2$ as a reference value in the estimation of the mesh spacing.

Equations (2), (6) and (7) provide means for estimating the mean mesh size in DNS and LES for turbulent RB convection. It should be noted that these estimations have been reached by plausibly assuming isotropic turbulence for unfiltered subgrid scales. They can be used as indicators for the mean mesh spacing, in particular, for the spatial resolution in the central region of the fluid layer, where even the resolved turbulence tends to be isotropic [8, 19]. Apart from these estimations, attention should also be paid to the vertical resolution, particularly in the near-wall thermal boundary layer, which is characterized by the thermal length scale, $\lambda_T \simeq H/Nu$ [23]. To resolve this layer, the mesh must be clustered in the vicinity of the wall to account for the large temperature gradient.

In the estimation using equations (2), (6) and (7), we have employed the scaling relations derived from DNS by Kerr [8]. These are $Nu = 0.186\,Ra^{0.276}$ and $\lambda_T = 5.9Ra^{-1/3}$. In equation (7), the dimensionless velocity scale u^* is determined from the resolved turbulence kinetic energy, K_c. Two velocity scales, u_{hc} and v_c, defined respectively from the center of the horizontal velocity, $u_h = (u_{\mathrm{rms}}^2 + w_{\mathrm{rms}}^2)^{1/2}$, and of the vertical velocity, v_{rms}, have been used to estimate K, namely, $K_c = (u_{hc}^2 + v_c^2)/2$. The scaling relations obtained from DNS analysis by Kerr [8] have been employed. These are $u_{hc}H/\alpha = 0.074Ra^{0.52}$ and $v_c H/\alpha = 0.25Ra^{0.46}$. For equation (7), these velocity scales indicate

$$u^* = \frac{\sqrt{K}H}{\alpha} = \sqrt{0.0027Ra^{1.04} + 0.0312Ra^{0.92}}. \tag{8}$$

Table 2 summarizes the estimated parameters associated with the grid resolution, which have been taken as references in generation of a set of refined meshes. Along with these estimated mean mesh spacings, the estimated Kolmogorov time scale, $\tau_k = (\nu/\varepsilon)^{1/2}$, has also been included in its dimensionless form, $\tau_k^* = \tau_k\alpha/H^2 = [(Nu-1)Ra]^{-1/2}$.

Based on the estimated parameters summarized in table 2, the mesh listed in table 1 may have underresolved the convective structures at large Ra numbers. New computations have thus been performed for the same range of Ra numbers, using the set of refined meshes shown in table 3, which have been generated on the basis of the above estimation and in the consideration of computational effectiveness. Referring to the estimated Kolmogorov time scale in table 2, the time step has been chosen using the standard CFL criterion with CFL ≤ 1.5 in general, as done in [8]. For reference, it is noted here that in the LES by Kimmel and Domaradzki

Table 2.   Estimated length scales and grid resolutions as references at different Rayleigh numbers.

Ra	6.3×10^5	10^7	4×10^7	10^8	10^9
η/H [equation (1)]	0.0188	0.0076	0.0049	0.0036	0.0017
τ_k^*	5.0×10^{-4}	8.20×10^{-5}	3.35×10^{-5}	1.85×10^{-5}	4.24×10^{-6}
h/H [equation (2)]	0.0590	0.0239	0.0153	0.0114	0.0054
R_{sgs} [in equation (6)]	1.0	2.0	3.0	4.0	5.0
Δ/H [equation (6)]	0.1084	0.0740	0.0641	0.0592	0.0335
$\lambda/2H$ [equation (7)]	0.1342	0.0834	0.0667	0.0577	0.0406
λ_T/H	0.0688	0.0274	0.0173	0.0127	0.0059

Table 3. Simulation parameters with refined grid resolutions.

Case	Ra	$N_x = N_z$	N_y	$\Delta x = \Delta z$	Δy_c	Δy_w	Δt
FA	6.3×10^5	96	64	0.0625	0.0301	0.0032	4.24×10^{-5}
FA1	6.3×10^5	72	64	0.0833	0.0301	0.0032	4.24×10^{-5}
FA2	6.3×10^5	72	64	0.0833	0.0301	0.0032	2.12×10^{-5}
FB	1.0×10^7	96	80	0.0625	0.0278	0.0021	2.13×10^{-6}
FC	4.0×10^7	128	96	0.0469	0.0263	0.0013	1.07×10^{-6}
FD	1.0×10^8	160	96	0.0375	0.0263	0.0013	0.68×10^{-6}
FD1	1.0×10^8	128	80	0.0469	0.0278	0.0021	0.68×10^{-6}
FE	1.0×10^9	176	128	0.0341	0.0249	0.0006	0.21×10^{-6}
FE1	1.0×10^9	176	128	0.0341	0.0249	0.0006	1.05×10^{-6}

[11], a $72 \times 129 \times 72$ mesh has been used for a $6 : 1 : 6$ domain at $Ra = 10^8$ using their SGS estimation model. Most recently, Kenjereš and Hanjalić [24] have performed a LES for RB convection at $Ra = 10^9$ on a $4 : 1 : 4$ domain meshed with $256 \times 128 \times 256$ cells, where the buoyancy-extended Smagorinsky model by Eidson [10] was employed with a constant model coefficient.

3. Results and discussion

We denote a fluctuating quantity of the resolved field as $\phi' = \bar{\phi} - \langle \bar{\phi} \rangle$ and $\phi_{\text{rms}} = \langle \phi'^2 \rangle^{1/2}$. The overbar, $(\bar{\cdot})$, indicates a filtered, resolved variable. To get the time-averaged turbulence statistics, a sufficiently long time period must be used to converge the time-averaged variables to statistically independent values. This has often been justified by the convective time scale [8, 18, 25]. We have used the same method as Kerr [8] in his DNS analysis. The convective time scale is roughly estimated by $t_c = 4H/u_c$, where $l = 4H$ is the distance around a single roll and u_c is the velocity scale taken from the center of the horizontal velocity [8]. Before starting to collect results for the statistic analysis, a time period of about 1–2 convective time scale is discarded until the resolved flow is fully developed. Figure 1 illustrates a typical example of the time-averaging history, which has been sampled at the center location of the domain. It is shown that the time-averaging process starts at about $t/t_c = 1.2$ for the resolved velocity component $\bar{u}$. The averaged values for $\bar{u}$ and $(\bar{u}\bar{u})$, namely, $\bar{u}_{\text{av}}$ and $(\bar{u}\bar{u})_{\text{av}}$, approach to statistically independent values with an increasing averaging time. For $\bar{u}_{\text{av}}$ in this example, it takes about $12t/t_c$ to reach $\bar{u}_{\text{av}} = \langle \bar{u} \rangle = 0$ at this location. The correlation, e.g. $(\bar{u}\bar{u})_{\text{av}}$, may reach a statistically independent value within a much shorter period, usually less than $5t/t_c$. In practice, the averaging time can be reduced significantly by additional spatial averaging over the horizontal homogeneous directions. In figure 2, the time-averaging history for the Nusselt number (see equation (9)) is illustrated for all the computed Rayleigh numbers at the center point of the domain. For Ra numbers below and at 4×10^7, the computations have been run for several tens of the convective time scale. At $Ra = 10^8$, the simulation has run for about $20t/t_c$ and about $12t/t_c$ for $Ra = 10^9$. All these time-averaging periods are much longer than those used in [8]. The resolved turbulence quantities presented below should be viewed as being statistically independent values.

We start with a brief analysis of the results sensitivity to the numerical resolution by comparing results for grids specified in tables 1 and 3. Note that all results have been normalized using H, $u_0 = \alpha/H$ and ΔT_0. A velocity component is thus expressed in terms of the Péclet number, $Pe = uH/\alpha$. At $Ra = 6.3 \times 10^5$ for vertical profiles, DNS data are available based
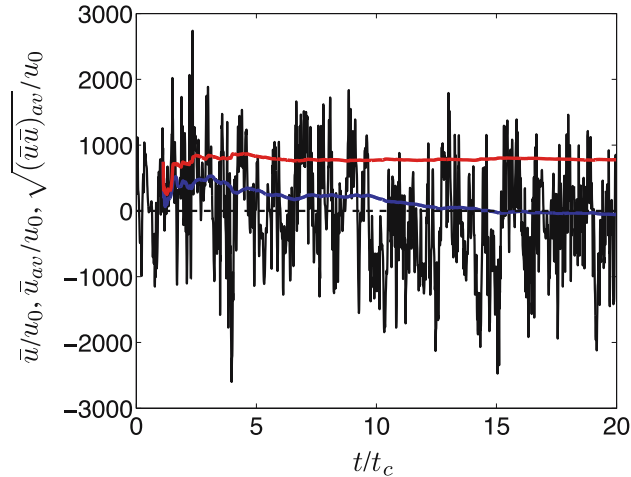
Figure 1.   Time history of the resolved velocity component $\bar{u}$ (black line), and time-averaging histories for $\bar{u}$, denoted $\bar{u}_{av}$ (blue line), and for $(\bar{u}\bar{u})$, denoted $(\bar{u}\bar{u})_{av}$ (red line). Probed at the central point of the domain for $Ra = 10^8$.

on a mesh resolution of $200 \times 49 \times 200$ on a $7.92 \times 1 \times 7.92$ domain [26], which have been included in the plotting where appropriate for comparison.

3.1   *Sensitivity of results to numerical resolution*

The set of coarse meshes, shown in table 1, has been used in our earlier work [19]. The mesh resolution was estimated using equation (6) by setting an estimated R_{sgs} that is generally derived from the resolution criteria used in LES for forced flows. For example, at $Ra = 10^9$, a value of $R_{sgs} \simeq 10$ was set for the resolution in case CE given in Table 1. It seems that for LES of turbulent thermal convections, this estimation of R_{sgs} at high Rayleigh numbers may lead to an insufficient resolution of the energetic thermal structures, of which the characteristic
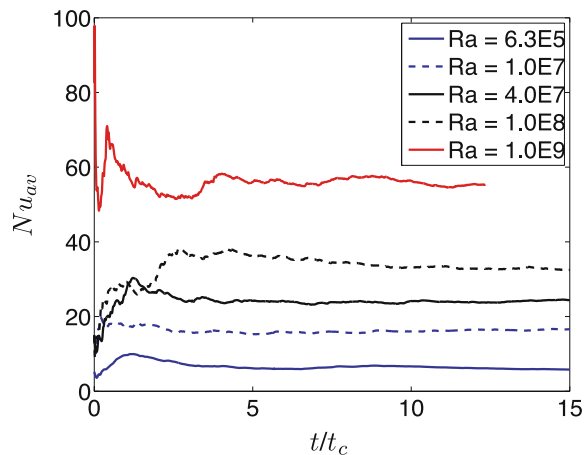
Figure 2.   Time-averaging histories for Nusselt number, *Nu*, at different Rayleigh numbers. Probed at the central point of the domain.

length scale is inversely proportional to Ra^β with $\beta > 0$. Indeed, the set of coarse meshes has underestimated the heat transfer [19], as compared with the previous experimental and DNS scaling relations. Effort has thus been made to investigate the effect of numerical resolution in terms of the mesh spacing and the time step with some comparisons between the cases given in Tables 1 and 3.

It is known that the SGS model in LES is closely related to the mesh spacing, for which the filtering cutoff, i.e. the filter width, has often been chosen as the characteristic length scale of SGS turbulence. The SGS modeling plays an essential role in representing the energy drain between the resolved large structure and the unresolved SGS structure. The more refined the grid, the less turbulence energy is contained in the unfiltered scales. A subsequent grid refinement will asymptotically drive a LES to DNS as the energy-carrying structures tend to be fully resolved. It should thus be recognized that the resolved flow quantities in LES may exhibit a dependence on grid refinement, very small though as the resolution is asymptotically approaching a DNS mesh. With a good SGS model and appropriate LES resolution, however, one can expect that the sum of a resolved flow quantity and its modeled SGS counterpart may present negligible grid dependence, for which the intensity of the SGS part should decrease while the resolved part may slightly increase with a grid refinement. Since the dynamic Smagorinsky model is used in the present computations, which is an eddy-viscosity-based model, the unfiltered SGS part cannot be retrieved from the modeled SGS contribution. Nevertheless, the turbulent heat flux across the fluid layer should be a relevant quantity as an indicator in analyzing the effect of grid resolution. The total turbulent heat flux, $\langle v'T' \rangle_{\text{tot}}$, is approximately the sum of the resolved heat flux, $\langle v'T' \rangle_{\text{res}}$, and the modeled SGS heat flux, $\langle h_{\theta 2} \rangle$, in the vertical y-direction, namely, $\langle v'T' \rangle_{\text{tot}} = \langle v'T' \rangle_{\text{res}} + \langle h_{\theta 2} \rangle$. Along with some other resolved turbulence statistics, the turbulent heat flux has thus been considered as an indicative variable in the following analysis of resolution sensitivity.

A comparison is made first for a relatively low Ra number, $Ra = 6.3 \times 10^5$, for which simulations have been performed with several meshes. These include a coarse-mesh case CA in table 1 and three refined-mesh cases FA, FA1 and FA2 in table 3. As seen, for all cases the resolution in the vertical direction, $N_y = 64$, has been kept the same, because it is even finer than the DNS resolution ($N_y = 49$) in [26]. From case CA to FA, the horizontal mesh resolution is doubled in both directions and the time step is reduced to a half. Cases FA1 and FA2 are used to investigate the effect of the time step, which have employed the same mesh but have doubled the time step in case FA1 compared to in case FA2. Figure 3 presents the resolved turbulence kinetic energy and the rms of temperature fluctuations in comparison with the DNS data. It is shown that the turbulence quantities have been resolved appropriately on the fine meshes, but somewhat underestimated with the coarse-mesh case CA.

Figure 4 presents the distributions for the resolved turbulent heat flux, $\langle v'T' \rangle_{\text{res}}$, and for the modeled SGS heat flux, $\langle h_{\theta 2} \rangle$. It is clearly demonstrated that the modeled heat flux is reduced with refined grid, while the resolved part increases marginally. The grid refinement from case CA to case FA induces only an increase of about 2% in the resolved turbulent heat flux in the center of the layer, whereas the maximum SGS heat flux has been reduced by about 50%. Moreover, it should be noted that, for cases FA1 and FA2 with the same grid resolution, different time steps have indeed imposed some effects on the resolved turbulence statistics, but the modeled SGS counterpart is hardly influenced. More interestingly, with a smaller time step in case FA2, the resolved heat flux computed on this coarser mesh becomes much closer to that with the finest mesh (case FA), in spite of the obvious difference in $\langle h_{\theta 2} \rangle$ for the two cases. This indicates the importance to resolve the evolution of convective, large-scale structures in time.
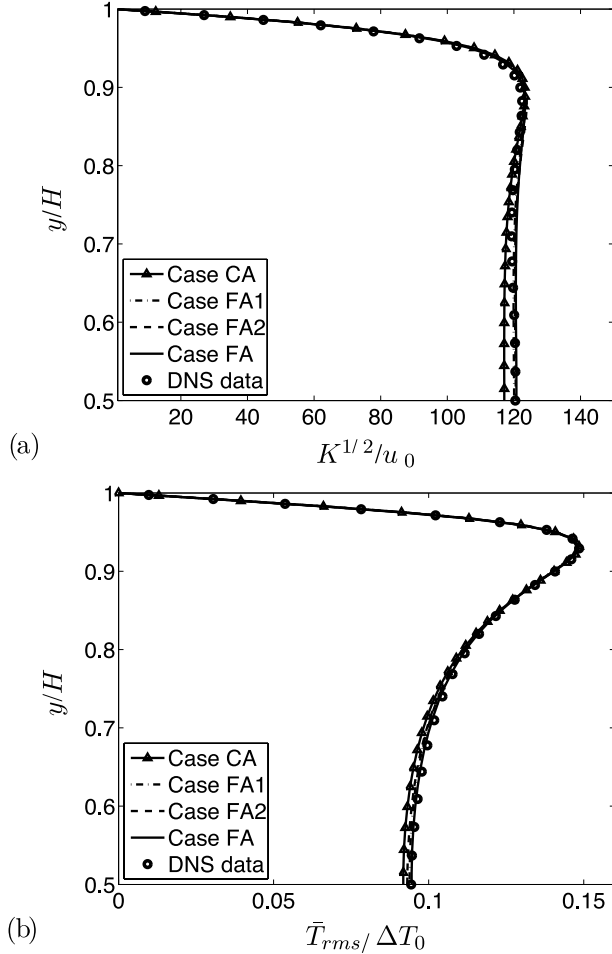
(a)

(b)

Figure 3. Effect of numerical resolution at $Ra = 6.3 \times 10^5$. (a) Resolved turbulence kinetic energy, $K = \left(\bar{u}_{\mathrm{rms}}^2 + \bar{v}_{\mathrm{rms}}^2 + \bar{w}_{\mathrm{rms}}^2 \right) / 2$. (b) Resolved temperature fluctuation.

In figure 5, the total turbulent heat flux, $\langle v'T' \rangle_{\mathrm{tot}} = \langle v'T' \rangle_{\mathrm{res}} + \langle h_{\theta 2} \rangle$, is plotted. For cases CA, FA, FA1 and FA2, the maximum peak value of $\langle h_{\theta 2} \rangle$ (arising at a distance of about $0.08H$ from the wall) is, respectively, about 11%, 8%, 8% and 6% of $\langle v'T' \rangle_{\mathrm{tot}}$ measured at the same location, and about 8%, 6%, 6% and 4% of the total heat transfer (the total turbulent heat flux plus the conductive heat transfer, see equation (9)). The grid convergence demonstrated in the prediction for the total turbulent heat flux suggests that, at $Ra = 6.3 \times 10^5$, the mesh resolution in case FA2 with a relevant time step has enabled a prediction of heat transfer that is grid insensitive. With the coarsest mesh, case CA, the prediction has already been reasonably accurate in view of the resolved turbulence statistics, for which this case underestimates the heat transfer by only about 2% as compared with case FA on the finest mesh.

The effect of mesh resolution is further addressed at $Ra = 10^8$ in figure 6. As shown in table 3, two meshes have been used with the same time step in cases FD and FD1, respectively. The vertical distributions for the total turbulent heat flux and for the modeled SGS heat flux are compared for these cases in figure 6, where the result computed with the coarse mesh (Case CD in table 1) has also been included. It is shown that the predicted $\langle v'T' \rangle_{\mathrm{tot}}$ has
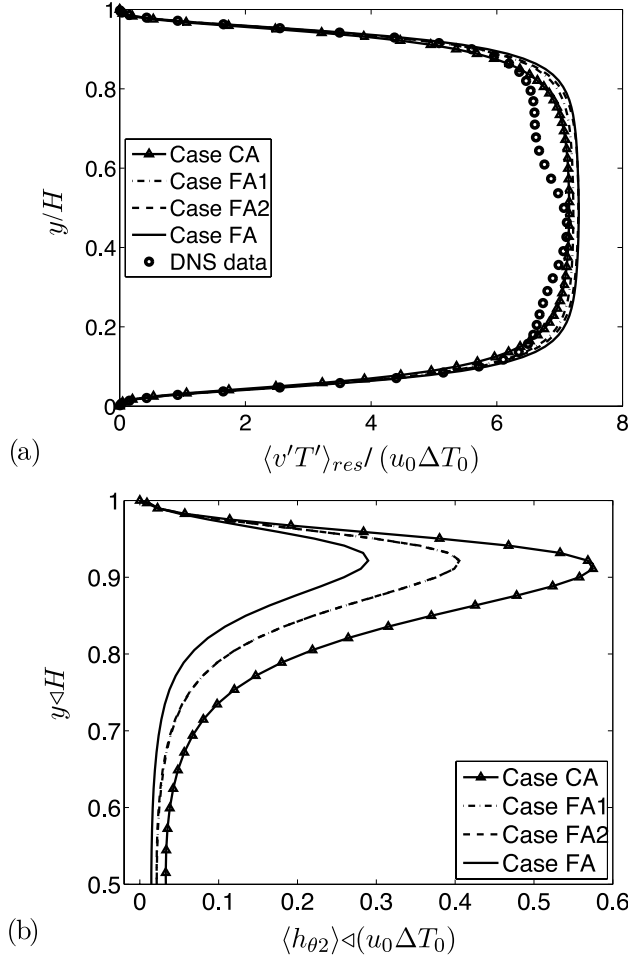
Figure 4. Effect of numerical resolution at $Ra = 6.3 \times 10^5$. (a) Resolved turbulent heat flux, $\langle v'T' \rangle_{\text{res}}$. (b) Modeled SGS heat flux, $\langle h_{\theta 2} \rangle$.

converged to almost identical distributions with the two refined meshes (cases FD and FD1). This indicates that the mesh resolution in FD1 has already been sufficient. Nonetheless, case CD has obviously underestimated the heat transfer as compared with the results from cases FD and FD1, about 14% lower in the center of the fluid layer.

At $Ra = 10^9$, along with the effect of mesh resolution refined from the coarse mesh (case CE in table 1) to the fine mesh (cases FE and FE1 in table 3) by ten times of the number of grid nodes, the effect of time step is also investigated. The time step in case FE is one-fifth of the time step used in case FE1 and one-tenth as in case CE. The predicted distributions of turbulent heat transfer are plotted in figure 7. Similar to the observation with cases FA1 and FA2 at $Ra = 6.3 \times 10^5$, a reduced time step hardly imposes any effect on the SGS heat flux when the same mesh is used as in cases FE and FE1 at $Ra = 10^9$. Nonetheless, a very slight difference (about 1%) can be observed in the resolved turbulent heat flux, and thus in the total turbulent heat flux as shown in figure 7(a). The turbulent heat transfer using the coarse mesh (case CE) has been significantly underestimated by about 21% relative to that produced using the refined mesh.
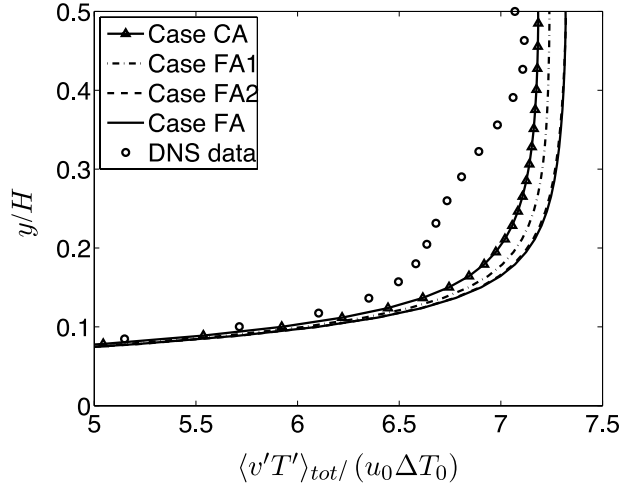
Figure 5. Effect of numerical resolution at $Ra = 6.3 \times 10^5$. The total turbulent heat flux, $\langle v'T' \rangle_{tot} = \langle v'T' \rangle_{res} + \langle h_{\theta 2} \rangle$. The distribution is zoomed in the low part where the most significant difference exists for different resolutions.
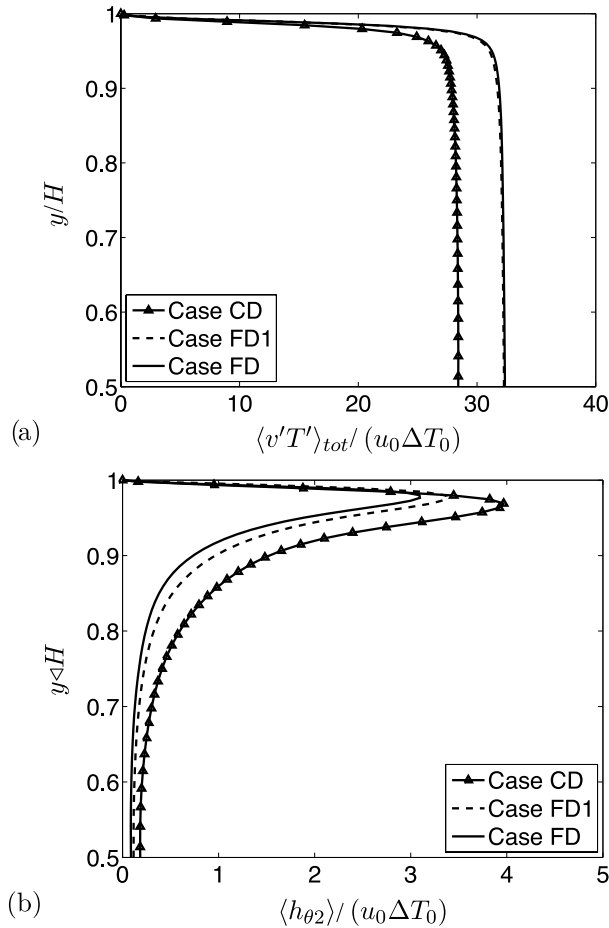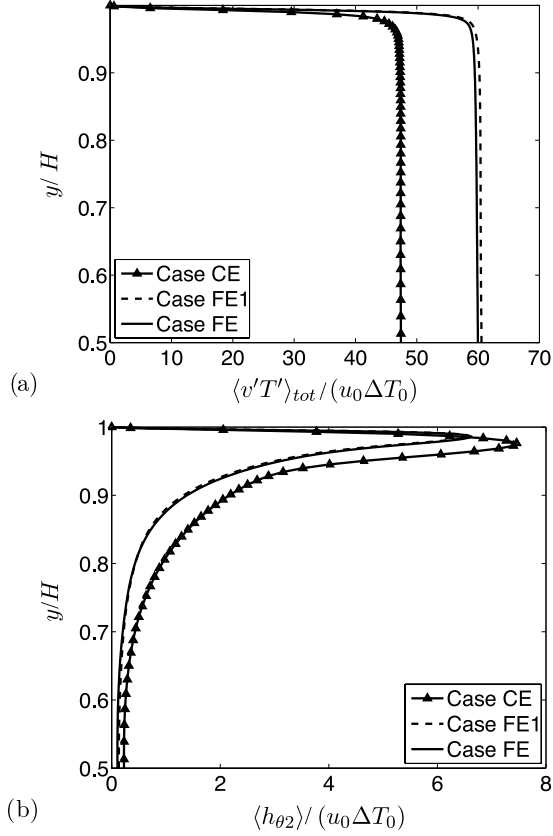

Figure 6. Effect of mesh resolution at $Ra = 10^8$. (a) Total turbulent heat flux, $\langle v'T' \rangle_{tot} = \langle v'T' \rangle_{res} + \langle h_{\theta 2} \rangle$. (b) Modeled SGS heat flux, $\langle h_{\theta 2} \rangle$.

Figure 7. Effect of numerical resolution at $Ra = 10^9$. (a) Total turbulent heat flux, $\langle v'T' \rangle_{\text{tot}} = \langle v'T' \rangle_{\text{res}} + \langle h_{\theta 2} \rangle$. (b) Modeled SGS heat flux, $\langle h_{\theta 2} \rangle$.

Based on the above sensitivity analysis of grid resolution and time step, it is recognized that the group of meshes in table 1 is too coarse at larger Ra numbers, and some time steps used may also have been too large to appropriately resolve the evolution of the filtered large-scale structures. With the group of refined meshes and time steps given in table 3, nonetheless, it is anticipated that well-resolved LES can be attained. In the following presentation of results and scaling analysis, only the results computed with the finest meshes and with the smallest time step are used, unless otherwise mentioned. These are cases FA, FB, FC, FD and FE.

3.2 *Turbulence statistics*

Before presenting the resolved turbulence statistics, a couple of illustrations are used to indicate the modeled SGS turbulence level. As mentioned, it is desirable in LES to resolve the turbulence energy as much as possible with the affordable costs and, so that the SGS turbulence tends to be isotropic, making SGS modeling more universal. In the present calculations, the Smagorinsky model has been used as the base model, which formulates the SGS eddy viscosity with $\nu_{\text{sgs}} = C_s \Delta |\bar{S}|^2$. The use of the dynamic procedure makes it possible to compute the model coefficient C_s as a function of local resolved flow properties. Figure 8(a) presents the distribution of the time-averaged model coefficient, C_s. In a large central part of the domain ($0.2 \leq y/H \leq 0.8$), this coefficient is located between 0.025–0.045, corresponding to a Smagorinsky constant,
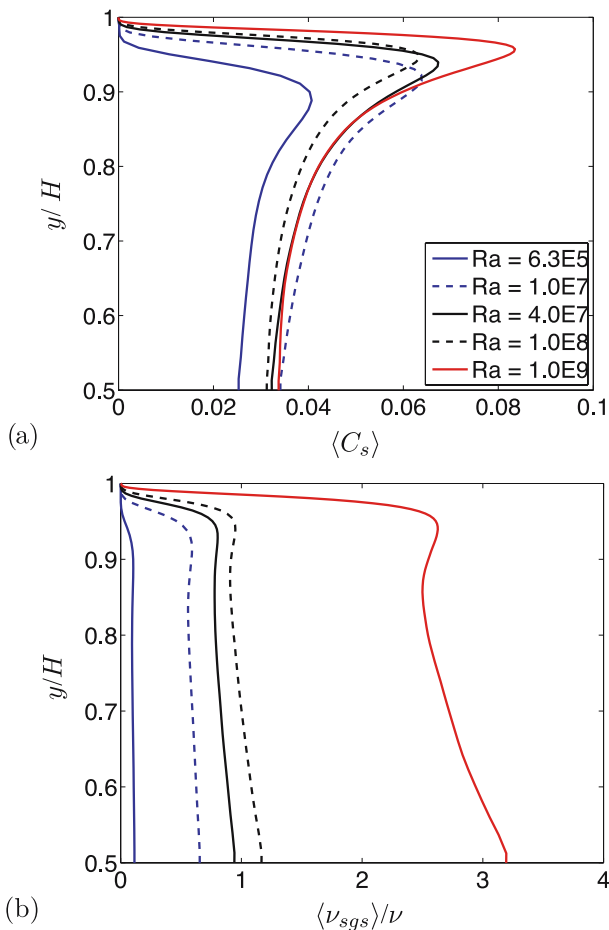
Figure 8.   (a) Time-averaged model coefficient, $\langle C_s \rangle$, computed from the dynamic procedure. (b) Time-averaged SGS eddy viscosity, $\langle \nu_{\mathrm{sgs}} \rangle / \nu$.

$\sqrt{C_s}$, of 0.16–0.21, which is in the range as determined by Lilly for homogeneous turbulence [27]. In the wall layer, however, C_s may reach a far larger value. At $Ra = 10^9$, the near-wall peak value is $C_{s,\mathrm{max}} = 0.085$, and $C_{s,\mathrm{max}} = 0.041$ for $Ra = 6.3 \times 10^5$. In figure 8(b), the time-averaged SGS eddy viscosity, $\langle \nu_{\mathrm{sgs}} \rangle$, is presented across the fluid layer. For $Ra \leq 4 \times 10^7$, $R_{\mathrm{sgs}} = \langle \nu_{\mathrm{sgs}} \rangle / \nu$ is generally less than 1. At $Ra = 10^8$, the maximum value of R_{sgs} is about 1.2, while this value raises to about 3.2 for $Ra = 10^9$ in the center of the fluid layer. Near the wall, where $C_{s,\mathrm{max}}$ is located, R_{sgs} is generally below 1, but $R_{\mathrm{sgs}} \simeq 2.7$ for $Ra = 10^9$. For $Ra = 6.3 \times 10^5$, the maximum value for R_{sgs} is about 0.12. As shown in the sensitivity analysis, the mesh used in case FA is indeed 'over-refined' for LES.

In figure 9, the time-averaged resolved temperature and the rms of temperature fluctuations are presented. At $Ra = 6.3 \times 10^5$, both the resolved temperature and its fluctuation are almost identical with the DNS data. It is shown that with increasing Ra number, the thickness of the thermal boundary layer, characterized by a near-wall sharp temperature gradient, is reduced. Correspondingly, the peak of the $\bar{T}_{\mathrm{rms}}$ distribution shifts toward the wall surface. The peak location of $\bar{T}_{\mathrm{rms}}$, λ_T, has been often used as the characteristic thickness of the wall thermal boundary layer. The centreline value of $\bar{T}_{\mathrm{rms}}$, namely, $\Theta_c = \bar{T}_{\mathrm{rms},c}$, is reduced obviously, as Ra
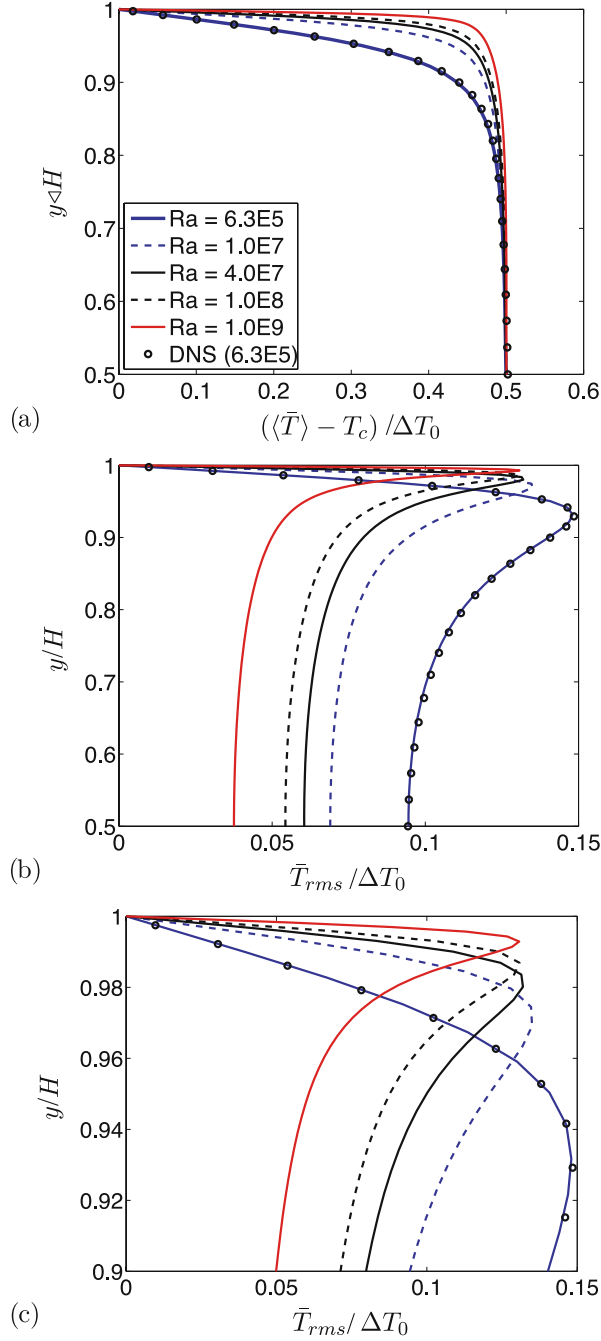
Figure 9. (a) Time-averaged resolved temperature, $(\langle \bar{T} \rangle - T_c)/\Delta T_0$. (b) Resolved temperature fluctuation, $\bar{T}_{\mathrm{rms}}/\Delta T_0$. (c) Close view of $\bar{T}_{\mathrm{rms}}/\Delta T_0$ near the wall.

number increases, while the near-wall peak value, $\Theta_w = \bar{T}_{\mathrm{rms,max}}$, exhibits a slight reduction with the increase in Ra number.

The heat flux across the fluid layer consists of three contributions when computed from an LES. These include the resolved turbulent heat flux, the modeled SGS part and the molecular
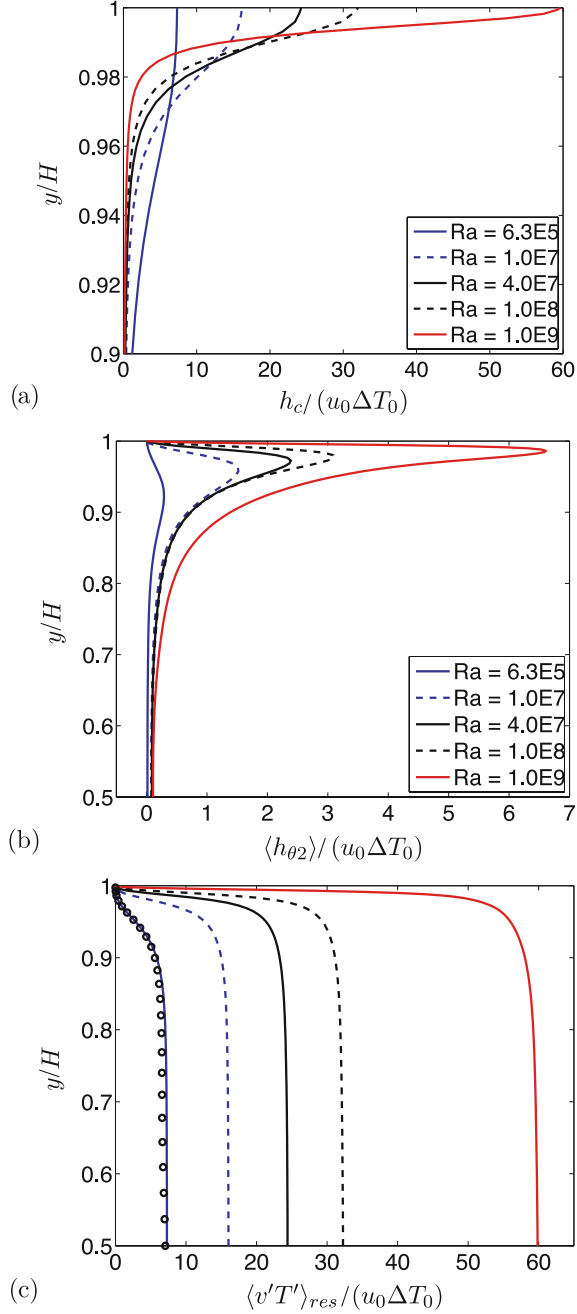
Figure 10. (a) Molecular diffusive heat transfer, $h_c = -\alpha \partial \langle \bar{T} \rangle / \partial y$. (b) SGS heat flux, $\langle h_{\theta 2} \rangle$. (c) Resolved turbulent heat flux $\langle v'T' \rangle_{\mathrm{res}}$. The symbol in (c) is the DNS data for $Ra = 6.3 \times 10^5$.

heat flux. The total heat transfer in its dimensionless form, namely the Nusselt number, reads

$$Nu(y) = \frac{\langle v'T' \rangle_{res} + \langle h_{\theta 2} \rangle - \alpha \partial \langle \bar{T} \rangle / \partial y}{\alpha \Delta T_0 / H}. \tag{9}$$

Figure 10 presents the distribution for the three heat transfer components. It is shown that the molecular diffusive heat flux is the main contributor to the total heat transfer in the vicinity of
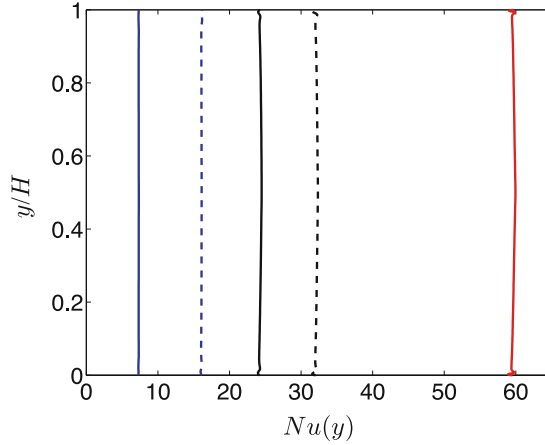
Figure 11. The total heat transfer cross the fluid layer, $Nu((y)$. Same legend as in figure 10.

the wall, but rapidly decreases with increasing Ra number, corresponding to an increasingly sharp near-wall temperature gradient. The SGS heat flux plays a role in the thermal boundary layer, from $Ra = 6.3 \times 10^5$ to the highest Rayleigh number ($Ra = 10^9$), the maximum SGS contributions (the peak value) to the total heat transfer are, respectively, 4%, 9.4%, 9.8%, 9.6% and 11%. Away from the wall, the heat transfer is dominated by the resolved turbulent heat flux.

In figure 11, the vertical distribution of $Nu(y)$ is presented. Since the horizontal direction is assumed to be homogeneous in the computation, the total heat flux is constant across the fluid layer at each Ra number. The smooth uniform distribution of $Nu(y)$ across the box has confirmed that the time used for averaging is sufficient in obtaining the statistically independent value of heat transfer.

In figure 12, the distributions for the rms of velocity fluctuations are presented. The two horizontal velocity components, $\bar{u}_{rms}$ and $\bar{w}_{rms}$, have been combined into a horizontal velocity, $u_{hrms} = (\bar{u}_{rms}^2 + \bar{w}_{rms}^2)^{1/2}$. The LES data show excellent agreement with the DNS data at $Ra = 6.3 \times 10^5$. With increasing Ra number, unlike the temperature fluctuation being weakened, the velocity fluctuation is reinforced. This is attributed to the motion of updraft and downdraft arising from the hot lower wall and descending from the cold upper wall, respectively. As the Ra number increases, these thermal plumes become intensified and impinge on the horizontal walls, causing notable horizontal motions. This has been reflected in the distribution of the horizontal velocity, u_{hrms}, which exhibits a near-wall peak, indicating the presence of near-wall shear. On the other hand, the vertical velocity, $\bar{v}_{rms}$, increases all the way from the wall to the center, as a consequence of the convective updrafts and downdrafts. Although not shown here, it is noted that the three velocity components at each Ra number have approximately similar values in the center of the box, which indicates that the turbulence tends to be isotropic in this region.

The resolved turbulence kinetic energy, $K = (u_{hrms}^2 + \bar{v}_{rms}^2)/2$, is also plotted in figure 12(c). The distribution of K presents a fairly flat distribution in a large part of the central mixed layer, but a small peak remains in the outer edge of the thermal boundary layer, particularly for $Ra \geq 4 \times 10^7$. The fact that the near-wall turbulence energy increases rapidly in the thermal boundary layer indicates that turbulence energy is transported by the thermal drafts. The horizontal rms velocity has a profile resembling that in a turbulent boundary layer, while $\bar{v}_{rms}$ increases all the way to the center. This reflects the fact that the near-wall shear layer and the
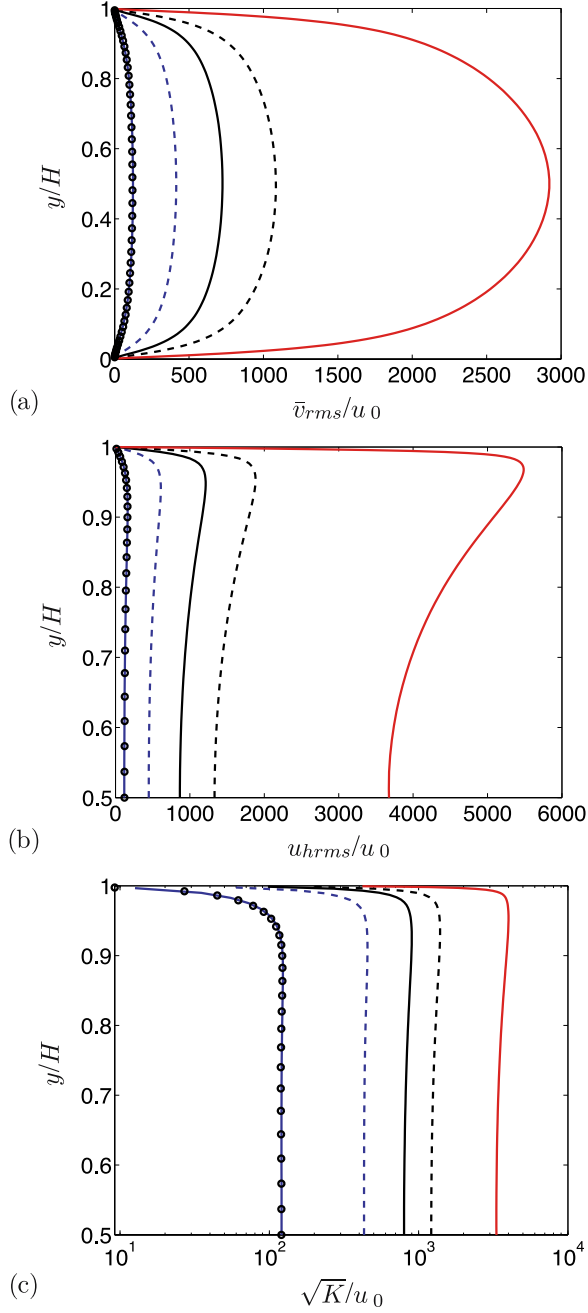
Figure 12.   (a) Resolved vertical velocity fluctuation, $\bar{v}_{\mathrm{rms}}/u_0$. (b) Resolved horizontal velocity fluctuation, u_{hrms}/u_0. (c) Resolved turbulence kinetic energy, $\sqrt{K}/u_0$. Same legend as in figure 9.

off-wall mixed layer co-exist in turbulent RB convection. The values of $\sqrt{K_c}$, as a velocity scale and taken from the center of the $\sqrt{K}$ distribution, will be scaled with the *Ra* number in the scaling analysis.

In addition, the centreline value and the near-wall peak value taken from the u_{hrms} distribution, as well as the centreline value of $\bar{v}_{\mathrm{rms}}$, denoted respectively by u_{hc}, u_{hw} and v_c, define

three characteristic velocity scales, of which the scaling relations with the *Ra* number will be revisited. Moreover, a length scale, λ_u, measured at the near-wall peak location of u_{hrms} to characterize the velocity boundary-layer thickness, is also scaled with the *Ra* number.

Figure 13(a) plots the skewness of the vertical velocity, $S_v = \langle v'^3 \rangle / \langle v'^2 \rangle^{3/2}$, which indicates the degree of asymmetry of the convective downdrafts and updrafts. Positive skewness implies that the vertical convection is characterized by relatively strong updrafts surrounded by weak downdrafts near the top cold wall, while negative skewness indicates intensive downdrafts surrounded by relatively weak updrafts near the bottom hot wall [16, 28]. Although not presented here, an illustration of the contour of instantaneous vertical velocities reveals that near the cold upper wall the updrafts (with positive v values) are separated from each other and surrounded by interconnected downdrafts (with negative v values). Near the hot lower wall, the situation is opposite, where individual downdrafts are surrounded by interconnected updrafts. A positive value of S_v indicates that the updraft from the lower hot wall has raised near the upper cold wall with high momentum and high kinetic energy, which penetrates locally into the cold thermal boundary layer and, with the aid of buoyancy, has made the cold fluid ejected locally from the wall layer in the form of relatively weak downdrafts. The updraft *presses* the cold thermal boundary layer toward the upper wall and leading to local positive vertical velocities. Near the lower wall surface, a similar situation occurs, where cold
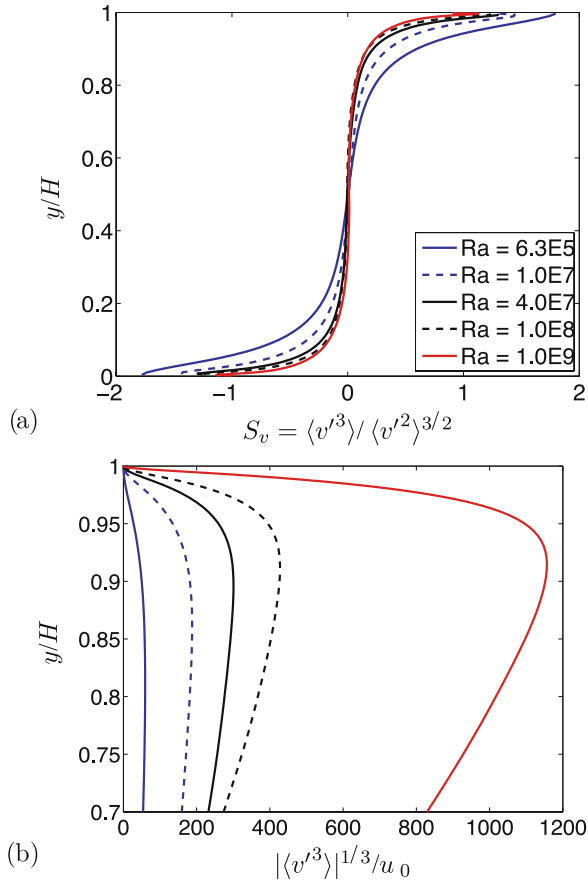

Figure 13.   (a) Skewness of vertical velocity. (b) Cubic root of the third central moment of vertical velocity, $\mu_3 = |\langle v'^3 \rangle|^{1/3}$. Note that the distribution of $\langle v'^3 \rangle$ is anti-symmetric with positive values near the upper cold wall, and negative in the lower part of the fluid layer.

plumes descending from the cold upper wall have caused local negative velocities, giving a negative S_v. This observation has been addressed previously by Moeng and Rotuno [28], and revisited by Kerr [8]. As *Ra* number increases, the near-wall skewness becomes smaller and the region with large skewness becomes thin. Across the center of the box the skewness profile approaches to a zero slope, which implies that the areas and the intensities of the updrafts and the downdrafts are similar over the nearly zero-slope layer. The convective updrafts and downdrafts alternatively co-exist in the box, which interact with (actually *suppress* or *contain*) each other due to their opposite motions. Both $\langle v'^2 \rangle$ and $\langle v'^3 \rangle$ have consisted of such an *inter-suppressing* feature. As a consequence, the skewness alone may not be sufficient to indicate the intensity of the dominant plume in the near-wall region. As shown in figure 12(a), the intensity of flow fluctuations is indicated by $\langle v'^2 \rangle$, which shows an increasingly sharp growth near the wall with increasing *Ra* number, in spite of the possible wall-damping effect on the approaching plume. On the other hand, the third moment, $\mu_3 = \langle v'^3 \rangle$, is able to indicate the direction of the dominant thermal plume. It is thus interesting to probe the near-wall distribution of μ_3, which can be viewed as an indicator of the intensity of the plume approaching the wall after being damped by the wall and being contained by the plume leaving the wall.

In figure 13(b), the distribution of $|\mu_3|^{1/3}/u_0$ is plotted. It should be noted that the distribution of $\langle v'^3 \rangle$ is anti-symmetric cross the box, with positive values in the upper part of the box, negative values in the lower part and zero in the center. We focus here on the near-wall maximum peak value of $\langle v'^3 \rangle$ and its distance to the wall. Figure 13(b) presents thus only a part of the distribution near the upper wall for $|\mu_3|^{1/3}$. With a negative sign, $\langle v'^3 \rangle$ has the same distribution in the lower part of the fluid layer. As shown, $|\mu_3|^{1/3}/u_0$ increases with increasing *Ra* number. At the same *Ra* number, $|\mu_3|$ increases from the center of the box to a peak value and then decreases to zero on the wall surface. The fact that the large near-wall value of S_v decreases with increasing *Ra* number indicates that the near-wall value of $\langle v'^2 \rangle^{1/2}$ is increasingly larger than $|\mu_3|^{1/3}$ as *Ra* number increases, that is, near the wall $(\langle v'^2 \rangle^{1/2} - |\mu_3|^{1/3})/u_0 \propto Ra^\beta (\beta > 0)$. This implies that the leaving plume becomes intensified with increasing *Ra* number and, as a result, the approaching plume is more contained by the leaving plume. In other words, the approaching plumes were contained from frequent penetrating into the viscous sublayer, as the *Ra* number is increased. The near-wall value of maximum $|\mu_3|$, defining a velocity scale as $u_{v3} = |\langle v'^3 \rangle|_{\max}^{1/3}$, and its distance to the wall, λ_{v3}, should thus be able to indicate some features of the interaction between the approaching and leaving drafts near the wall. The velocity scale, u_{v3}, represents the intensity of the approaching plume after being contained by the leaving plume. The length scale, λ_{v3}, may indicate the *turning point*, at which the leaving plume starts to play a significantly sensible role in containing further growth of the intensity of the approaching plume. Kerr [8] has argued that the incoming/approaching plume and negative S_v may be an important ingredient in producing the shear, which may be associated with the hard convective turbulence. In the following *Ra*-scaling analysis, the velocity scale, u_{v3}, and the length scale, λ_{v3}, will be accommodated.

Furthermore, in order to observe the intensity of wall shear, figure 14 plots the time-averaged magnitude of the resolved flow strain rate, $\langle |\bar{S}| \rangle = \langle \sqrt{2\bar{S}_{ij}\bar{S}_{ij}} \rangle$, where $\bar{S}_{ij} = (\partial \bar{u}_i/\partial x_j + \partial \bar{u}_j/\partial x_i)/2$. It is shown that across a large central portion of the box, $\langle |\bar{S}| \rangle$ is relatively small and has a uniform distribution, yet its value on the wall, S_w, is rather large, implying significant wall shear.

The centreline value, S_c, and the wall value, S_w, of $\langle |\bar{S}| \rangle$ are taken in the following scaling analysis. Note that S_c and S_w have a reciprocal dimension of a time scale. The sharp change of $\langle |\bar{S}| \rangle$ from S_w to S_c near the wall indicates the existence of a shear layer in the vicinity of the wall. By means of the $|\bar{S}|$ distribution, we define a new length scale to characterize the
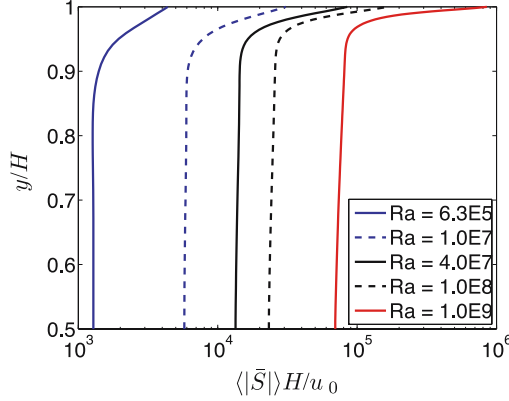
Figure 14.   Time-averaged magnitude of resolved flow strain rate.

thickness of the near-wall shear layer, namely

$$\lambda_s = \frac{\int_0^H \langle |\bar{S}| \rangle \mathrm{d}y - S_c H}{S_w - S_c}.$$ (10)

This length scale will be addressed in the following scaling analysis.

3.3   *Rayleigh-number scaling*

Using the statistically averaged properties discussed in the previous section, we have analyzed the *Ra*-scaling for the range of Rayleigh numbers where LES has been performed, namely, $Ra \in [6.3 \times 10^5, 10^9]$. Note that the *Ra* range considered includes the transition regime (at $Ra_{\mathrm{tr}} \approx 4 \times 10^7$) from soft to hard turbulence observed in some experiments [6]. As noted earlier, from the DNS for $Ra \le 2 \times 10^7$ by Kerr [8] it was found that a single regime corresponding to the hard convective scaling can be established to represent the *Ra* dependence, being applicable for the heat transfer and several velocity and temperature scales.

Based on the present LES results, the main purpose of the *Ra*-scaling analysis is twofold: scrutinizing the scaling relations for *Ra* numbers covering the soft and hard turbulence regimes using the present LES computations, and comparing the LES results with the experimental and DNS-derived scaling laws. With the present LES data and assuming a single-scaling relation for each characteristic scale, the best-fitted *Ra*-scaling relations are summarized in tables 4 and 5.

Figure 15 plots the Nusselt number, *Nu*, versus the *Ra* number. Note that the Nusselt number can be calculated at the wall by $Nu_w = -H \langle \partial \bar{T}/\partial y \rangle_w / \Delta T_0$. Both the integrated $Nu(y)$ (from equation (9)) and Nu_w have been included in figure 15, showing negligible difference. The scaling does not exhibit any notable transition at $Ra_{\mathrm{tr}} = 4 \times 10^7$ that would otherwise separate different regimes (soft and hard) with different scaling. The LES data for the five *Ra* numbers

Table 4.   *Ra*-scaling of flow and thermal quantities with a relation of CRa^β for each. Note that the superscript * denotes being normalized by u_0, H and ΔT_0.

	u_{hw}^*	u_{hc}^*	v_c^*	$\sqrt{K_c^*}$	Θ_w^*	Θ_c^*	S_w^*	S_c^*	u_{v3}^*	$u_{\tau w}^*$	Nu
C	0.279	0.235	0.405	0.30	0.182	0.501	0.301	0.857	0.287	0.520	0.162
β	0.478	0.468	0.429	0.45	−0.0172	−0.123	0.717	0.549	0.40	0.358	0.286

Table 5.   *Ra*-scaling of the length scales with a relation of CRa^{β} for each.

	λ_u/H	λ_T/H	λ_s/H	λ_{v3}/H
C	0.609	4.549	0.458	0.85
β	-0.142	-0.313	-0.146	-0.116

considered all collapse on a single curve for which the least square fit gives $Nu = 0.162Ra^{0.286}$. This correlation corresponds closely (apart from slightly larger heat transfer) to the 2/7 (hard turbulence) scaling observed experimentally by Wu and Libchaber [6] only for $Ra \geq 4 \times 10^7$, and supports the DNS findings of [8] that the hard scaling applies in the 'numerical thermal convection' at much lower Ra numbers, deep in the soft turbulence range of experimental convection. The present LES data confirm the hard-scaling correlation validity to higher Ra numbers, at least to $Ra = 10^9$.

The normalized temperature rms, $\Theta_w = \bar{T}_{\text{rms,max}}$ and $\Theta_c = \bar{T}_{\text{rms,center}}$, are plotted in figure 16, together with the scaling relations derived from DNS data (for $Ra \leq 2 \times 10^7$) by Kerr [8], where $\Theta_c/\Delta T_0$ and $\Theta_w/\Delta T_0$ were *forced* to fit with the $Ra^{-1/7}$ and $Ra^{-1/14}$ laws, respectively. As shown, the LES data are in large discrepancies from these *forced* scaling relations. Instead, the LES data for $\Theta_w/\Delta T_0$ agree better with the DNS data obtained at lower Ra numbers (cf figure 11 in [8]). Similar to the DNS data, with increasing Ra number, LES produces temperature fluctuations much less steep near the wall than in the center. The near-wall $\Theta_w/\Delta T_0$ presents a moderate reduction at lower Ra numbers. As Ra number increases from $Ra \geq 4 \times 10^7$, $\Theta_w/\Delta T_0$ seems to approach a constant value of about 0.131, showing an almost decoupled Ra dependence. This can also be seen from figure 9. With the theoretical scaling laws, $\Theta_c/\Delta T_0 \sim Ra^{-1/9}$ and $Ra^{-1/7}$ for soft and hard convective turbulence, respectively, $\Theta_c/\Delta T_0$ shows a fairly good agreement. The varied tendencies presenting respectively in the scaling relations for $\Theta_w/\Delta T_0$ and $\Theta_c/\Delta T_0$ suggest that there indeed exist some transition features in these scales separated at about $Ra = 4 \times 10^7$ from soft to hard turbulence regime, as indicated by the experiment [6].
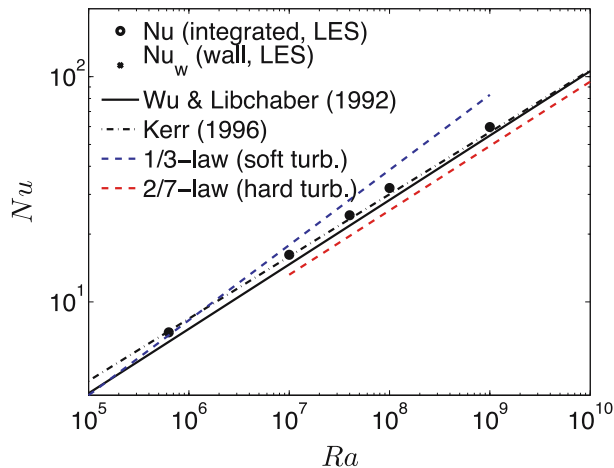

Figure 15.   Nusselt number versus *Ra* number. The LES data gives $0.162Ra^{0.286}$. Also plotted are the experimental *Ra*-scaling $0.146Ra^{0.286}$ by Wu and Libchaber [6] and the DNS *Ra*-scaling $0.186Ra^{0.276}$ by Kerr [8].
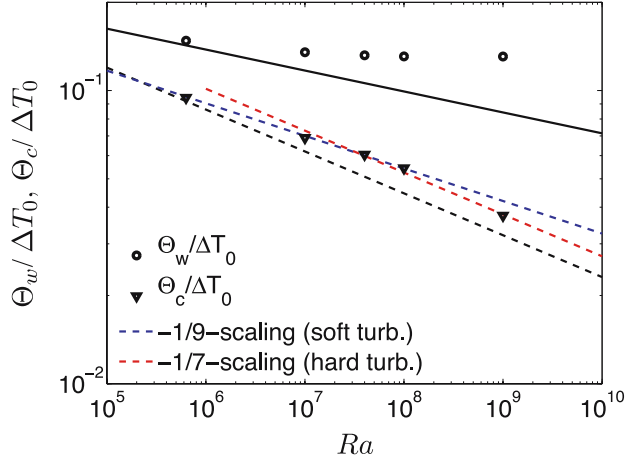
Figure 16. *Ra* dependence of $\bar{T}_{rms}$ in the center, $\Theta_c/\Delta T_0$, and at the near-wall peak, $\Theta_w/\Delta T_0$. The LES data fit with $\Theta_w/\Delta T_0 = 0.182Ra^{-0.0172}$ and $\Theta_c/\Delta T_0 = 0.501Ra^{-0.123}$, respectively. Black solid line indicates the *forced* DNS *Ra*-scaling by Kerr [8] for $\Theta_w/\Delta T_0 = 0.37Ra^{-1/14}$, and black dashed line for $\Theta_c/\Delta T_0 = 0.62Ra^{-1/7}$.

In figure 17, the normalized velocity scales defined from the rms of vertical and horizontal velocity fluctuations are plotted versus the *Ra* number. The LES gives, respectively, $u_{hw}/u_0 = 0.279Ra^{0.478}$, $u_{hc}/u_0 = 0.235Ra^{0.468}$ and $v_c/u_0 = 0.405Ra^{0.429}$. In the range of lower *Ra* numbers with DNS [8], it was shown that u_{hc}/u_0 has a somewhat smaller value than the other two, whereas the present LES data disclose generally smaller values for v_c/u_0. In addition, the DNS data for u_{hw}/u_0 and v_c/u_0 are collapsed closely so the two scales were fitted with an identical scaling relation in [8]. This is not the case with the LES data. Instead, the two velocities, u_{hc}/u_0 and v_c/u_0 in the center of the box are closer, but with an increasing
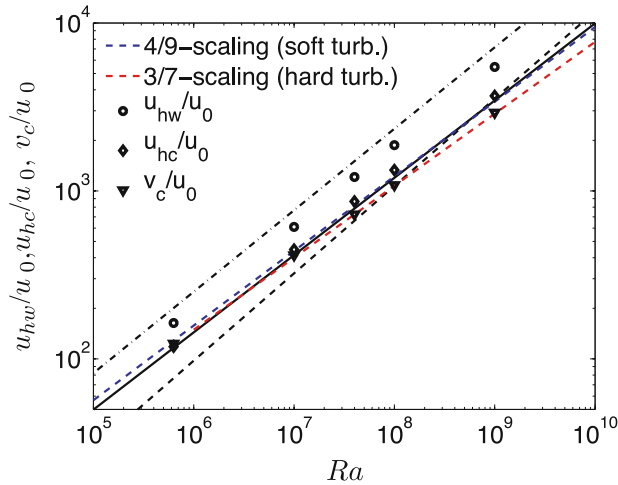

Figure 17. *Ra* dependence of near-wall peak value, u_{hw}/u_0, of u_{hrms}, and the scales, u_{hc}/u_0 and v_c/u_0, taken from the center of distributions for u_{hrms} and v_{rms}, respectively. The LES data give $u_{hw}/u_0 = 0.279Ra^{0.478}$, $u_{hc}/u_0 = 0.235Ra^{0.468}$ and $v_c/u_0 = 0.405Ra^{0.429}$. Black solid line is the DNS *Ra*-scaling by Kerr [8] for both u_{hw}/u_0 and v_c/u_0 with $0.25Ra^{0.46}$, and black dashed line for $u_{hc}/u_0 = 0.074Ra^{0.52}$. The black dash-dotted line is from the experiment by Sano et al. [5] in a confined vertical cylinder with an aspect ratio of 1, giving $Pe = 0.309Ra^{0.485}$ for the mean vertical velocity.

difference as Ra number increases. The scaling relation for v_c/u_0 fit very well with the 3/7-law for hard turbulence [1, 23], while the data for u_{hc}/u_0 fit closer to the 4/9-law for soft convective turbulence. The scaling taken from the experiment by Sano et al. [5] is for the mean vertical velocity (not fluctuations) measured in a confined vertical cylinder with an aspect ratio of 1. It was stated that this velocity can be scaled with $Ra^{0.46}$, if the Pr number dependence is not neglected. In calculating this velocity based on the measured cross spectrum from paired bolometers, they have assumed that the vertical velocity is much larger than the horizontal velocity. If the effect of the horizontal velocity is included, this experimentally measured scaling relation should be modified and would become closer to the LES data. In addition, Kerr [8] suggested a check on the consistency of scales with $Nu - 1 \leq (\Theta_c/\Delta T_0)(v_c/u_0)$ by a Cauchy inequality. The LES data give $(Nu - 1) = 0.1125Ra^{0.3035}$, which complies with the inequality. With the Ra dependence of these velocity scales, there is no obvious indication on the transition from soft to hard convective turbulence.

Figure 18 presents the scaling relations with the LES data for another two normalized velocity scales, $u_{v3}^* = |\langle v'^3 \rangle_{\max}|^{1/3}/u_0$ and $u_{\tau w}/u_0$, respectively. The former is taken from the near-wall maximum value of the triple correlation for the vertical velocity fluctuations, and the latter has been calculated as a wall-friction velocity by $u_{\tau w} = \sqrt{\nu \partial u_{\text{hrms}}/\partial y|_{\text{wall}}}$. In addition, the scale taken from the resolved turbulence kinetic energy, $\sqrt{K_c}$, in the center of the box is also presented, which can be viewed also as a velocity scale for the resolved large-scale structure. All these quantities increase with increasing Ra number. The LES data give $\sqrt{K_c}/u_0 = 0.30Ra^{0.45}$, $u_{\tau w}/u_0 = 0.520Ra^{0.358}$ and $u_{v3}^* = 0.287Ra^{0.40}$. The scaling for $\sqrt{K_c}/u_0$ has an exponent of about 4/9, which is the theoretical scaling exponent for soft turbulence [1]. Of these three velocity scales, u_{v3}^* is the only one which has shown a slight shift from a single-scaling relation, and presenting better matching with scaling exponents for the soft and hard turbulence regimes separated at $Ra = 4 \times 10^7$.

The two characteristic boundary-layer thicknesses ('heights'), λ_u and λ_T, measured at the locations with maximum values of $u_{\text{h rms}}$ and $\bar{T}_{\text{rms}}$, respectively, are plotted in figure 19. As with DNS, LES shows that λ_u is generally larger than λ_T for $Ra \geq 6.3 \times 10^5$. The LES data give $\lambda_u/H = 0.609Ra^{-0.142}$ and $\lambda_T/H = 4.549Ra^{-0.313}$, which comply reasonably well with the DNS scaling relations that agree with soft-turbulence scaling for λ_T/H and hard-turbulence
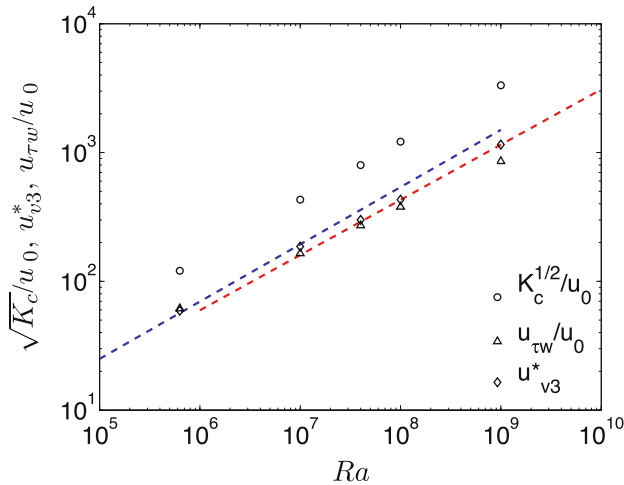

Figure 18. Ra dependence of $\sqrt{K_c}/u_0$, $u_{v3}^* = |\langle v'^3 \rangle|_{\max}^{1/3}/u_0$ and $u_{\tau w}/u_0$. The LES data give $\sqrt{K_c}/u_0 = 0.30Ra^{0.45}$, $u_{\tau w}/u_0 = 0.520Ra^{0.358}$ and $u_{v3}^* = 0.287Ra^{0.40}$. The blue dashed line indicates the 4/9-scaling for soft turbulence and the red dashed line represents the 3/7-scaling for hard turbulence [1].
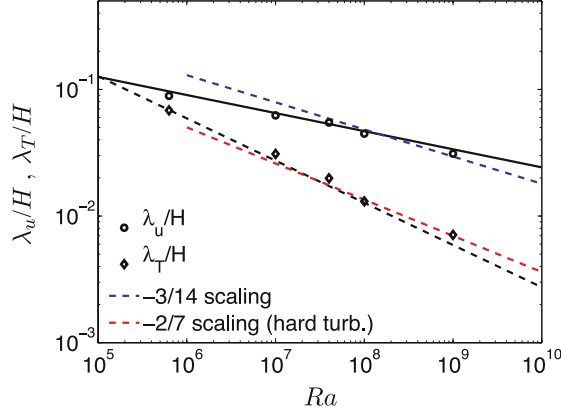
Figure 19. *Ra* dependence of λ_u/H and λ_T/H. LES data give $\lambda_u/H = 0.609Ra^{-0.142}$ and $\lambda_T/H = 4.549Ra^{-0.313}$. Black solid line indicates DNS *Ra*-scaling by Kerr [8] for $\lambda_u/H = 0.65Ra^{-1/7}$, and black dashed line for $\lambda_T/H = 5.9Ra^{-1/3}$.

scaling for λ_u/H. Nonetheless, if the scaling exponent $(-2/7)$ for hard turbulence regime is plotted for λ_T/H (the red dashed line in figure 19), it shows an even better fitting with the LES data than the $(-1/3)$ scaling for large *Ra* numbers, whereas the Thomae scaling exponent $(-3/14)$ matches fairly well with the LES data of λ_u/H. The $(-1/3)$ scaling does not match well in the soft-turbulence regime for λ_u/H, however. In summary, the thermal length scale, λ_T, may match with two scaling relations for the soft and hard turbulence regimes, respectively. The velocity length scale, λ_u, exhibits somewhat an offset from a single-scaling relation at $Ra = 4 \times 10^7$ and matches reasonably well with $(-1/7)$ scaling for lower *Ra* numbers and with $(-3/14)$ scaling for larger *Ra* numbers.

In figure 20, the wall (S_w) and centreline (S_c) values of $\langle|\bar{S}|\rangle$ are plotted. Both are best fitted respectively with a single-scaling relation. These are $S_w H/u_0 = 0.301Ra^{0.717}$ and $S_c H/u_0 = 0.857Ra^{0.549}$. It should be noted that the scaling of $u^*_{\tau w} \sim Ra^{\beta_{u\tau}}$ can be related to the scaling of $S^*_w \sim Ra^{\beta_{Sw}}$ with $\beta_{Sw} \approx 2\beta_{u\tau}$, as is shown in table 4. Note that $\langle|\bar{S}|\rangle$ is a reciprocal time scale, which might be used together with an appropriate velocity scale to derive a length scale that can be used to examine the computational resolution of large-scale structures in RB convection.
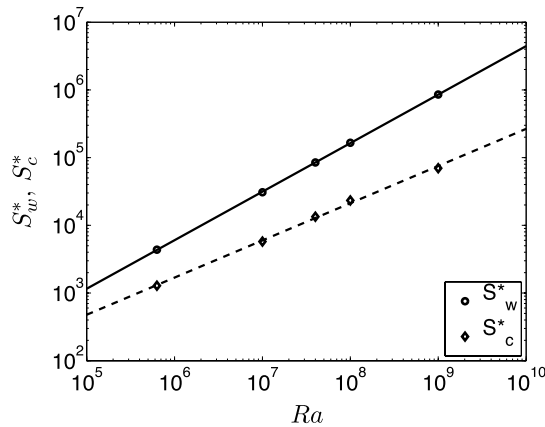

Figure 20. *Ra* dependence of $\langle|\bar{S}|\rangle$ on the wall and in the center. LES data give $S^*_w = S_w H/u_0 = 0.301Ra^{0.717}$ and $S^*_c = S_c H/u_0 = 0.857Ra^{0.549}$, which are represented by the solid line and dashed line, respectively.

The scaling for λ_s and λ_{v3}, defined respectively by equation (10) and from the location of the near-wall maximum value of $\langle v'^3 \rangle$, is shown in figure 21. With a single-scaling relation for each, the LES computation gives $\lambda_s/H = 0.458Ra^{-0.146}$ and $\lambda_{v3}/H = 0.85Ra^{-0.116}$. The scaling exponent for λ_s/H is close to $(-1/7)$, which is the scaling law for λ_u in the hard-turbulence regime [1]. Note that λ_s is a characteristic thickness for the near-wall shear layer, which is comparable with λ_u but decreases slowly relative to λ_u with increasing Ra number, indicating the additional effect of vertical motions on $|\bar{S}|$. In general, λ_{v3} is measured outside of the near-wall diffusive sublayer, which at the same Ra number is larger than the other length scales defined in this work. As shown in figure 21, λ_{v3} decreases relatively fast for $Ra \le 4 \times 10^7$, after which its reduction with increasing Ra number becomes smaller. As shown in the near-wall distribution of $|\langle v'^3 \rangle|^{1/3}$ in figure 13(b)), λ_{v3} represents the location at which the approaching plume has grown to its maximum intensity. Being damped by the wall and contained by the leaving plume, at this characteristic wall distance the vertical approaching plume tends to be re-directed to horizontal motions. This length scale separates two layers. The near-wall layer is a *damping layer*, where the incoming/approaching plume is mainly damped by the wall and somewhat contained by the leaving plume, but its intensity is still statistically dominant over the leaving plume (and thus positive $\langle v'^3 \rangle$ near the cold upper wall and negative near the hot bottom wall). From the outer edge of this layer ($\sim \lambda_{v3}$) toward the wall up to a distance characterized by λ_u, the horizontal motion tends to be formed and reinforced, the approaching plume being gradually re-directed to the horizontal direction. In the layer with a thickness of λ_u, the horizontal motion is dominant and is affected by wall shear. In the outer layer, the intensity of the approaching plume keeps growing toward the wall but also being contained sensibly by the leaving plume. With increasing Ra number, one would expect a reducing λ_{v3} due to the increasing intensity of the approaching plume. But this is not the case at large Ra numbers after $Ra = 4 \times 10^7$, the reduction in λ_{v3} becomes instead much slower with increasing Ra number. This is because the intensity of the leaving plume becomes at large Ra numbers increasingly strong in containing the approaching plume from penetrating toward the wall surface. The shift in the scaling relation for λ_{v3}/H after about $Ra = 4 \times 10^7$ may thus be attributed to the leaving plume, of which the intensity increases with increasing Ra number and imposing increasing containing effect on the approaching plume. This has consequently, together with the wall-damping effect, stopped its further penetration toward the wall.
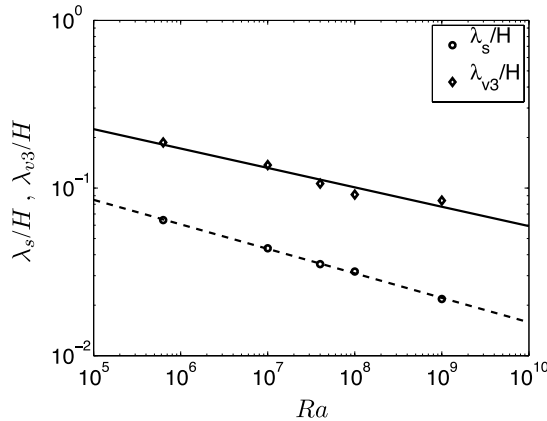

Figure 21. *Ra* dependence of λ_s/H and λ_{v3}/H. The LES data fit $\lambda_s/H = 0.458Ra^{-0.146}$ and $\lambda_{v3}/H = 0.85Ra^{-0.116}$, which are plotted by the dashed and solid lines, respectively.

4. Conclusions

LES with the dynamic Smagorinsky SGS model has been performed for turbulent Rayleigh–Bénard convection for $Ra \in [6.3 \times 10^5, 10^9]$, covering the experimentally observed transition regime from soft to hard convective turbulence. *A priori* analysis of the grid resolution requirements and *a posteriori* grid sensitivity test using several grid densities demonstrate that the finest grids used provided sufficient resolution for trustworthy LES. To attain accurate LES predictions of heat transfer, the SGS heat flux accounts for only about 10% (or below) of the total heat flux. The vertical distributions of the resolved turbulence statistics demonstrate Ra dependence similar to the available DNS and experimental data. The scaling relations derived from the present LES data have been shown to be in reasonable agreement with the existing scaling laws.

The convective updrafts ascending from the hot wall and downdrafts descending from the cold wall have been argued as being the main engine to generate and account for the vertical profiles and the magnitudes of turbulence quantities. As the Ra number is increased, wall shear becomes reinforced while the thickness of the shear layer decreases due to intensified horizontal motions caused by the collision of the vertical draft with the wall. The interaction of both downdraft and updraft causes increasingly intensive velocity fluctuations in both the vertical and horizontal directions with increasing Ra numbers. The thermal fluctuation, on the other hand, is suppressed by opposite buoyant sheets which are surrounded by vertical drafts stemmed from the opposite wall. The intensities of both the leaving plume and the incoming/approaching plume increase, as the Ra number is increased, but the increase for the leaving plume is more effective than for the approaching plume which is also damped by the wall. When the Ra number is increased to about 4×10^7, the leaving plume becomes much intensified so that it is able, together with the wall-damping effect, to significantly contain the approaching plume and, consequently, alleviating its penetration toward the wall. This is reflected in the near-wall distributions of the rms, the skewness and the triple correlation of the vertical velocity fluctuations and, in particular, indicated by the small variation in the location of $|\langle v'^3 \rangle|_{\max}^{1/3}$ at large Ra numbers. The length scale, λ_{v3}, is argued as being the characteristic location, where the approaching plume is significantly contained and damped and, consequently, a local balance may set up between the intensities of the approaching plume and the leaving plume. Moving further toward the wall, at a distance characterized by λ_u (or similarly by λ_s), the approaching plume is redirected to horizontal motions and the flow is affected by wall shear.

In the Rayleigh-scaling analysis, a number of scales, defined from the computed vertical profiles, have been revisited in comparison with existing experimental and DNS results. Apart from the scales conventionally used in previous experimental and theoretical analysis, several new scales have also been defined and analyzed. Among others, these include the length scales λ_s and λ_{v3} and the velocity scale u_{v3}. For the heat transfer, the LES data agrees well with previous DNS analysis, and is best-fitted with $Nu = 0.162 Ra^{0.286}$. The scaling exponent is identical with previous experimental data for the scaling in the hard-turbulence regime. Most characteristic scales, derived from the LES data for 'numerical RB convection', can be fitted reasonably well with a single relation for each, with no obvious change in regimes from soft to hard convective turbulence at the transitional Ra number (about $Ra = 4 \times 10^7$) identified in previous experiments.

Nonetheless, there exist several characteristic quantities, of which the scaling shows indeed a sensible offset from a single relation at about $Ra = 4 \times 10^7$, but being fitted better with two separate scaling relations. These include the temperature scales Θ_w and Θ_c, the velocity scale u_{v3}, and the length scales λ_{v3}, λ_u and λ_T. The scaling relations for $\Theta_c/\Delta T_0$, u_{v3}/u_0 and λ_T/H have shown fairly good matching with the scaling laws for soft convective turbulence at low Ra

numbers and for hard turbulence at large *Ra* numbers, in consistency with previous theoretical analysis and experimental observation. These 'transition-sensitive' quantities, derived from 'numerical convection', are probably scales that are less sensitive to the side-wall effect encountered in 'experimental convection'. Instead, they are more closely associated to the effect of horizontal motions near the top and bottom walls, as well as to the interaction between the updraft and the downdraft. The transition observed in the scales defined from the near-wall region is related to the near-wall 'containing effect' of the increasingly (with *Ra* number) intensified plume leaving the wall on the approaching plume. As the *Ra* number increases to $Ra = 4 \times 10^7$ and larger, at a wall distance characterized by λ_{v3}, the leaving plume, together with the wall-damping effect, significantly alleviates the penetration of the approaching plume into the wall layer.

Acknowledgments

References

[1] Castaing, B., Gunaratne, G., Heslot, F., Kadanoff, L., Libchaber, A., Thomae, S., Wu, X., Zaleski, Z. and Zanetti. G., 1989, Scaling of hard thermal turbulence in Reyleigh–Bérnard convection. *Journal of Fluid Mechanics*, **204**, 1–30.
[2] Siggia, E.D., 1994, High Rayleigh number convection. *Annual Review of Fluid Mechanics*, **26**, 137–168.
[3] Bodenschatz, E., Pesch, W. and Ahlers, G., 2000, Recent development in Rayleigh–Bénard convection. *Annual Review of Fluid Mechanics*, **32**, 709–778.
[4] Deardorff, J.W. and Willis, G.E., 1967, Investigation of turbulent thermal convection between horizontal plates. *Journal of Fluid Mechanics*, **28**, 453–480.
[5] Sano, M., Wu, X.Z. and Libchaber, A., 1989, Turbulence in helium-gas free convection. *Physical Review A*, **40**, 6421–6430.
[6] Wu, X.Z. and Libchaber, A., 1992, Scaling relation in thermal turbulence: the aspect-ratio dependence. *Physical Review A*, **45**, 842–845.
[7] Chu, T.Y. and Goldstein, R.J., 1973, Turbulent convection in a horizontal layer of water. *Journal of Fluid Mechanics*, **60**, 141–160.
[8] Kerr, M.R., 1996, Rayleigh number scaling in numerical convection. *Journal of Fluid Mechanics*, **310**, 139–179.
[9] Kerr, M.R. and Herring, J.R., 2000, Prandtl number dependence of Nusselt number in direct numerical simulations. *Journal of Fluid Mechanics*, **419**, 325–344.
[10] Eidson, T.M., 1985, Numerical simulation of the turbulent Rayleigh–Bénard problem using subgrid modelling. *Journal of Fluid Mechanics*, **158**, 245–268.
[11] Kimmel, S.J. and Domaradzki, J.A., 2000, Large eddy simulations of Rayleigh–Benárd convection using subgrid scale estimation model. *Physics of Fluids*, **12**, 169–184
[12] Kenjereš, S. and Hanjalić, K., 1999, Transient analysis of Rayleigh–Bénard convection with a RANS model. *International Journal of Heat and Fluid Flow*, **20**, 329–340.
[13] Kenjereš, S. and Hanjalić, K., 2002, Numerical insight into flow structure in ultra-turbulent thermal convection. *Physical Review E*, **66**, 1–5.
[14] Germano, M., Piomelli, U., Moin, P. and Cabot, W.H., 1991, A dynamic subgrid-scale eddy viscosity model. *Physics of Fluids A*, **3**, 1760–1765.
[15] Lilly, D.K., 1992, A proposed modification of the Germano subgrid-scale closure method. *Physics of Fluids A*, **4**, 633–635.
[16] Peng, S.-H. and Davidson, L., 1998, Comparison of subgrid-scale models in LES for turbulent convection flow with heat transfer. In *Turbulent Heat Transfer 2*, p. 5.24–5.35 (UK: Manchester).
[17] Hartlep, T., Tilgner, A. and Busse, F.H., 2003, Large scale structures in Rayleigh–Bénard convection at high Rayleigh numbers. *Physical Review Letters*, **91**, 064501–1–4.
[18] Hartlep, T., Tilgner, A. and Busse, F.H., 2005, Transition to turbulent convection in a fluid layer heated from below at moderate aspect ratio. *Journal of Fluid Mechanics*, **554**, 309–322.
[19] Peng, S.-H., Davidson, L. and Hanjalic, K., 2005, Numerical analysis of Rayleigh–Bénard convection using large eddy simulation at high Rayleigh numbers. In *Proceedings of 4th International Symposium on Turbulence and Shear Flow Phenomena*, vol. 3, pp. 983–988.
[20] Grötzbach, G., 1982, Direct numerical simulation of laminar and turbulent Bénard convection. *Journal of Fluid Mechanics*, **119**, 27–53.

[21] Grötzbach, G., 1983, Spatial resolution requirement for direct numerical simulation of Rayleigh–Bénard convection. *Journal of Computational Physics*, **49**, 241–264.

[22] Sagaut. P., 1998, *Large eddy simulation for incompressible flows*. Springer, Berlin Heidelberg.

[23] Shraiman B.I., and Siggia, E.D., 1990, Heat transport in high-Rayleigh-number convection. *Physical Review A*, **42**, 3650–3653.

[24] Kenjereš, S. and Hanjalić, K., 2005, LES, T-RANS and hybrid simulations of thermal convection at high Ra numbers. In *Engineering Turbulence Modelling and Experiments VI* (Amsterdam: Elsevier), pp. 369–378.

[25] Werne, J., DeLuca, E.E., Rosner, R. and Cattaneo. F., 1991, Development of hard-turbulent convection in two-dimensions: numerical evidence. *Physical Review Letters*, **67**, 3519–3522.

[26] Wörner, M., 1994, Direkte simulation turbulenter Rayleigh–Bénard konvektion in fluessigem natrium. Dissertation, University of Karlsruhe, KfK 5228, Kernforschungszentrum Karlsruhe.

[27] Lilly, D.K., 1967, The representation of small-scale turbulence in numerical simulation experiments. In *Proceedings on IBM Scientific Computation on Environmental Science* (NY: Yorktown Hights).

[28] Moeng, C.-H., and Rotunno, R., 1990, Vertical-velocity skewness in the buoyancy-driven boundary layer. *Journal of Atmospheric Sciences*, **47**, 1149–1162.